

See discussions, stats, and author profiles for this publication at: <https://www.researchgate.net/publication/222415244>

# Structure of Amantadine-Bound M2 Transmembrane Peptide of Influenza A in Lipid Bilayers from Magic-Angle-Spinning Solid-State NMR: The Role of Ser31 in Amantadine Binding

ARTICLE *in* JOURNAL OF MOLECULAR BIOLOGY · JANUARY 2009

Impact Factor: 4.33 · DOI: 10.1016/j.jmb.2008.11.022

---

CITATIONS

103

---

READS

49

3 AUTHORS, INCLUDING:



**Tatiana V Mishanina**

University of Wisconsin–Madison

8 PUBLICATIONS 144 CITATIONS

SEE PROFILE



**Mei Hong**

Iowa State University

152 PUBLICATIONS 6,185 CITATIONS

SEE PROFILE



# Structure of Amantadine-Bound M2 Transmembrane Peptide of Influenza A in Lipid Bilayers from Magic-Angle-Spinning Solid-State NMR: The Role of Ser31 in Amantadine Binding

Sarah D. Cady, Tatiana V. Mishanina and Mei Hong\*

Department of Chemistry,  
Iowa State University, Ames,  
IA 50011, USA

Received 12 August 2008;  
received in revised form  
6 November 2008;  
accepted 12 November 2008  
Available online  
24 November 2008

The M2 proton channel of influenza A is the target of the antiviral drugs amantadine and rimantadine, whose effectiveness has been abolished by a single-site mutation of Ser31 to Asn in the transmembrane domain of the protein. Recent high-resolution structures of the M2 transmembrane domain obtained from detergent-solubilized protein in solution and crystal environments gave conflicting drug binding sites. We present magic-angle-spinning solid-state NMR results of Ser31 and a number of other residues in the M2 transmembrane peptide (M2TMP) bound to lipid bilayers. Comparison of the spectra of the membrane-bound apo and complexed M2TMP indicates that Ser31 is the site of the largest chemical shift perturbation by amantadine. The chemical shift constraints lead to a monomer structure with a small kink of the helical axis at Gly34. A tetramer model is then constructed using the helix tilt angle and several interhelical distances previously measured on unoriented bilayer samples. This tetramer model differs from the solution and crystal structures in terms of the openness of the N-terminus of the channel, the constriction at Ser31, and the side-chain conformations of Trp41, a residue important for channel gating. Moreover, the tetramer model suggests that Ser31 may interact with amantadine amine via hydrogen bonding. While the apo and drug-bound M2TMP have similar average structures, the complexed peptide has much narrower linewidths at physiological temperature, indicating drug-induced changes of the protein dynamics in the membrane. Further, at low temperature, several residues show narrower lines in the complexed peptide than the apo peptide, indicating that amantadine binding reduces the conformational heterogeneity of specific residues. The differences of the current solid-state NMR structure of the bilayer-bound M2TMP from the detergent-based M2 structures suggest that the M2 conformation is sensitive to the environment, and care must be taken when interpreting structural findings from non-bilayer samples.

© 2008 Elsevier Ltd. All rights reserved.

Edited by A. G. Palmer III

**Keywords:** influenza M2 proton channel; solid-state NMR; chemical shifts; magic-angle spinning; amantadine

\*Corresponding author. E-mail address: [mhong@iastate.edu](mailto:mhong@iastate.edu).

Abbreviations used: M2TMP, M2 transmembrane peptide; OG, octyl- $\beta$ -D-glucopyranoside; SSNMR, solid-state NMR; MAS, magic-angle spinning; DHPC, 1,2-dihexadecyl-*sn*-glycero-3-phosphatidylcholine; DLPC, 1,2-dilauroyl-*sn*-glycero-3-phosphatidylcholine; DMPC, 1,2-dimyristoyl-*sn*-glycero-3-phosphatidylcholine; POPC, 1-palmitoyl-2-oleoyl-*sn*-glycero-3-phosphatidylcholine; DMPG, 1,2-dimyristoyl-*sn*-glycero-3-phosphatidyl-glycerol; MD, molecular dynamics; DQF, double-quantum-filtered; COSY, correlated spectroscopy; PDB, Protein Data Bank.

## Introduction

The M2 protein of influenza A virus forms a tetrameric proton channel that is the target of the anti-viral drugs amantadine and rimantadine.<sup>1</sup> The drugs were effective until recently, when a single-site mutation of S31N in the transmembrane domain of the protein caused complete resistance of the viruses to the drugs.<sup>2</sup> The M2 proton channel is important for viral replication. After the virus enters the infected cell by endocytosis, the proton channel acidifies the viral core, which triggers the dissociation of the virus matrix and subsequent viral gene expression.<sup>3</sup> With 97 amino acids, the M2 protein is small compared to typical ion channels; thus, it is an excellent system for elucidating the structure–function relationship of ion channels. Extensive mutagenesis, electrophysiological,<sup>4,5</sup> and sedimentation experiments<sup>6</sup> have been carried out to determine the low-resolution structure and stability of this proton channel. Elucidating the high-resolution structure and the difference between the drug-free and drug-bound states is the next natural challenge that is important not only for developing new inhibitors to curb influenza infection but also for understanding the fundamental biophysics of ion channels.

The transmembrane domain of the M2 protein spanning residues 22 to 46 (Fig. 1a) contains a histidine and a tryptophan that are crucial for proton conduction and gating.<sup>8,9</sup> This domain exhibits channel activity<sup>10</sup> and forms a parallel four-helix bundle with left-handed crossing angles. The resi-

dues facing the channel lumen *versus* the lipids have been identified through experiments probing the effects of mutation on proton currents and amantadine inhibition.<sup>11</sup> The main channel-facing residues, V27, A30, G34, and H37, fall onto the *a* and *d* positions of a heptad repeat (Fig. 1b). The *b*, *c*, and *f* positions of the heptad repeat face the lipids, while the *e* and *g* positions occupy the helix–helix interfaces. Apart from the transmembrane domain, the segment of the protein spanning residues 44–60 forms a membrane-proximal amphipathic helix that is important for channel stability<sup>12</sup> and is recently found to be involved in pH activation.<sup>13</sup>

Recently, two high-resolution structures of portions of the M2 protein containing the transmembrane domain were reported simultaneously.<sup>14,15</sup> One structure was obtained by X-ray crystallography and the other by solution NMR. The X-ray structure was determined on amantadine-bound M2 (22–46) in the detergent octyl- $\beta$ -D-glucopyranoside (OG).<sup>15</sup> The solution NMR structure was determined on rimantadine-bound M2(18–60) solubilized in 1,2-dihexadecyl-*sn*-glycero-3-phosphatidylcholine (DHPC) micelles.<sup>14</sup> Strikingly, the two structures showed very different drug binding sites: the solution NMR structure showed rimantadine to be bound at the helix–helix interfaces of the tetramer near the C-terminus of the transmembrane domain, while the crystal structure showed amantadine bound to the channel lumen near the N-terminus. In addition, the helix orientation and the side-chain conformations of the two structures differ substantially.<sup>16</sup>

These structural differences underscore the importance of examining the M2 transmembrane peptide (M2TMP) structure using an independent technique and doing so in the most biologically relevant environment of lipid bilayers. Detergent micelles are known to cause curvature stress to membrane proteins and have been documented to affect the structure of proteins compared to bilayer-bound samples.<sup>17</sup> Similarly, crystallizing hydrophobic membrane proteins in a sparse matrix of detergent molecules leaves open the question of how different the structure is from the bilayer-bound state. For these reasons, solid-state NMR (SSNMR) spectroscopy, which can be readily applied to lipid bilayers and other semisolids, is the preferred method for determining the high-resolution structures of membrane proteins.

Until recently, the majority of SSNMR data on the M2TMP consisted of static <sup>15</sup>N chemical shift anisotropies and N–H dipolar couplings measured on uniaxially aligned membrane samples. These data yielded very precise orientation angles of the M2TMP helices in the lipid bilayer.<sup>18,19</sup> However, the <sup>15</sup>N NMR constraints do not report the side-chain conformation or the interhelical packing of the tetramer. Further, information on the backbone structure is only inferred by pattern recognition of the 2D N–H dipolar and <sup>15</sup>N chemical shift correlation spectra.

We recently undertook a magic-angle-spinning (MAS)-SSNMR study of the structure and dynamics

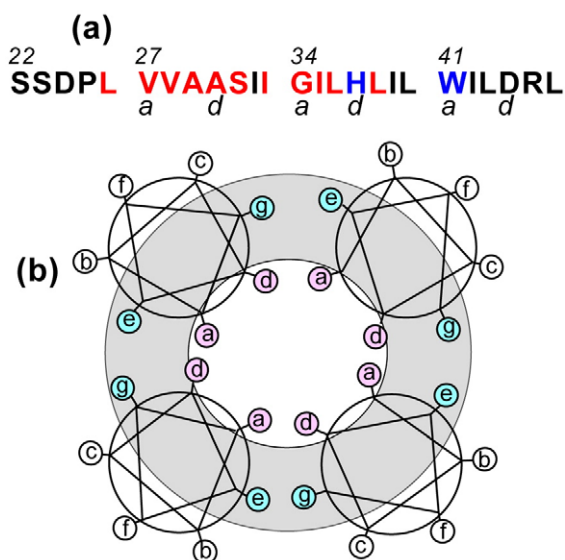


**Fig. 1.** M2(22–46) sequence and its representation as a heptad repeat. (a) Amino acid sequence. The *a* and *d* residues of the heptad repeat *abcdefg* are labeled. The <sup>13</sup>C, <sup>15</sup>N-labeled residues that have been studied so far<sup>7</sup> are colored red. H37 and W41, which are central for proton conduction and channel gating, are shown in blue. (b) Four-helix bundle organization of M2TMP. Channel-facing *a* and *d* residues are shaded pink, and interfacial *e* and *g* residues are shaded cyan.

of M2(22–46) in lipid bilayers. Several types of structural information have been obtained so far. First, isotropic  $^{13}\text{C}$  and  $^{15}\text{N}$  chemical shifts of eight residues in the transmembrane domain (L26, V27, A29, A30, I33, G34, I35, and L38) were measured and compared between the apo and amantadine-complexed states<sup>7</sup> to determine structure perturbation by the drug. Second,  $\phi$ ,  $\psi$ , and  $\chi_1$  torsion angles were directly measured at selected residues by dipolar correlation experiments to quantify the peptide conformation. Third, we measured the helix orientations using unoriented membrane samples and found small differences between the apo and drug-bound peptide, as well as different tilt angles in lipid bilayers of different thicknesses.<sup>20,21</sup> Fourth, the peptide dynamics were probed by  $^2\text{H}$  quadrupole NMR and various dipolar coupling and chemical shift anisotropy measurements and were found to be dramatically altered by drug binding.<sup>20</sup> Finally, we measured interhelical distances at V27, A30, L38, and W41 using  $^{19}\text{F}$ -labeled M2TMP to constrain the helix packing in the tetrameric bundle.<sup>22,23</sup> These SSNMR results were obtained from M2TMP bound to hydrated and unoriented 1,2-dilauroyl-*sn*-glycero-3-phosphatidylcholine (DLPC), 1,2-dimyristoyl-*sn*-glycero-3-phosphatidylcholine (DMPC), or 1-palmitoyl-2-oleoyl-*sn*-glycero-3-phosphatidylcholine (POPC) membranes, which are more natural environments for membrane proteins than detergents.

In this work, we report the chemical shifts of Ser31, Val28, and Leu36 and propose a backbone structural model of M2TMP using all SSNMR constraints obtained so far. Ser31 has been postulated to be the main residue involved in amantadine binding. Molecular dynamics (MD) simulations suggested that the Ser31 hydroxyl group forms hydrogen bonds with the amantadine amine.<sup>24</sup> This was supported by neutron diffraction experiments that showed amantadine to be positioned between Val27 and Ser31.<sup>25</sup> Mutation of Ser31 to Asn gives rise to the main drug-resistant mutant in current influenza A viruses. Thus, knowledge of Ser31

conformation in M2TMP is important for understanding how amantadine blocks the channel. The availability of chemical shifts for a contiguous segment of the peptide allows us to deduce the ( $\phi$ ,  $\psi$ ) torsion angles of the protein using the well-established relation between protein conformation and NMR chemical shifts.<sup>26</sup> From this chemical-shift-constrained monomer structure, we constructed a tetramer model of the transmembrane domain using several interhelical distances measured previously. We compare this MAS-NMR model with the solution NMR, X-ray, and  $^{15}\text{N}$  orientation-NMR structures and suggest the binding site of amantadine.

## Results

### $^{13}\text{C}$ chemical shifts of VSL-M2TMP without and with amantadine

Figure 2 shows the lipid-suppressed  $^{13}\text{C}$  MAS spectra of V28-, S31-, and L36-labeled M2TMP without (Fig. 2a and c) and with (Fig. 2a and d) amantadine. The lipid background signals were suppressed by a  $^{13}\text{C}$ – $^{13}\text{C}$  DQ filter in Fig. 2a and b and a  $^{15}\text{N}$ – $^{13}\text{C}$  heteronuclear dipolar filter in Fig. 2c and d. For the N–C-filtered spectra, only the directly bonded  $\text{C}^\alpha$  signals are selected due to the short N–C recoupling time used. All spectra were measured at 243 K, in the gel phase of the membrane.

The main  $^{13}\text{C}$  chemical shift difference caused by amantadine occurs at S31  $\text{C}^\alpha$  and  $\text{C}^\beta$ : the two sites overlap completely in the apo M2TMP spectrum (Fig. 2a) but become partly resolved in the amantadine-complexed spectrum (Fig. 2b). In addition, the  $^{15}\text{N}$ – $^{13}\text{C}$ -filtered spectra in Fig. 2c show a narrower S31  $\text{C}^\alpha$  peak for the complexed peptide than the apo peptide. At low temperature where peptide motion is frozen, NMR linewidths reflect conformational distribution. Thus, the narrower  $\text{C}^\alpha$  line of the complexed peptide indicates reduced conforma-

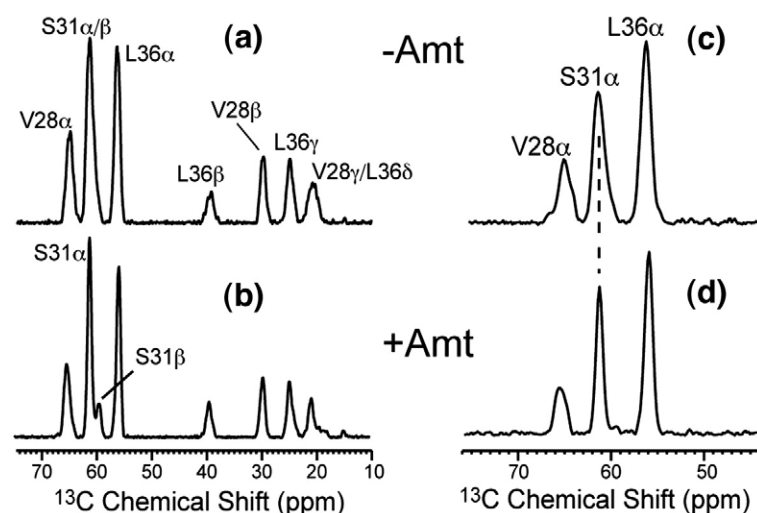


**Fig. 2.** 1D  $^{13}\text{C}$  spectra of VSL-M2TMP in DLPC bilayers at 243 K. (a)  $^{13}\text{C}$  DQF spectrum of the apo peptide. (b)  $^{13}\text{C}$  DQF spectrum of the amantadine-bound peptide. (c)  $^{15}\text{N}$ -filtered  $^{13}\text{C}$  spectrum of the apo peptide. (d)  $^{15}\text{N}$ -filtered  $^{13}\text{C}$  spectrum of the amantadine-bound peptide.



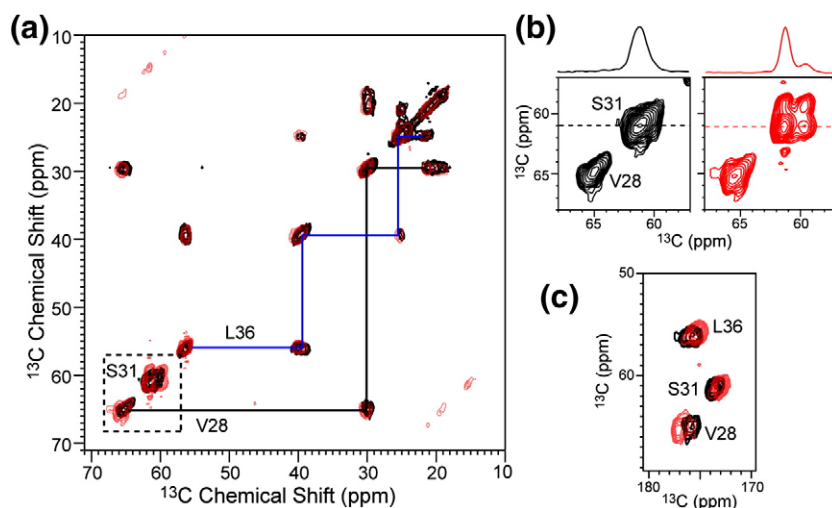


**Fig. 3.** 2D  $^{13}\text{C}$ - $^{13}\text{C}$  DQF correlation spectra of VSL-M2TMP in DLPC bilayers at 243 K without (black) and with (red) amantadine. (a) Aliphatic region. (b) S31 and V28 region. (c) Carbonyl region.

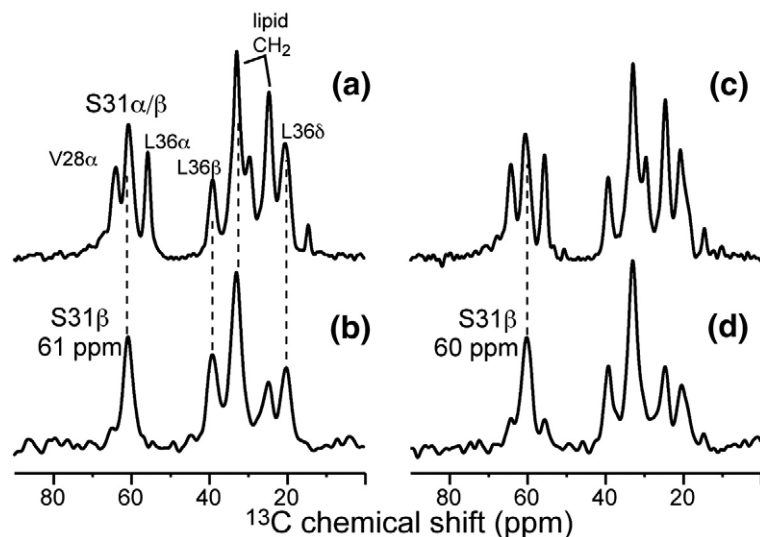
tional heterogeneity at S31 upon drug binding (see below).

Figure 3 shows the 2D  $^{13}\text{C}$ - $^{13}\text{C}$  double-quantum-filtered (DQF) correlated spectroscopy (COSY) spectra to illustrate the unambiguous assignment of the  $^{13}\text{C}$  chemical shifts. The 2D spectra further illustrate the striking difference of S31 chemical shifts between the apo and amantadine-complexed M2TMP: while the apo peptide does not resolve the S31  $\text{C}^\alpha$  and  $\text{C}^\beta$  peaks near 61 ppm, the complexed peptide shows clear off-diagonal intensities indicative of chemical shift separation between  $\text{C}^\alpha$  and  $\text{C}^\beta$  (Fig. 3b). On the other hand, the S31  $\text{C}^\alpha/\text{CO}$  cross peaks are unchanged by amantadine (Fig. 3c). Since protein secondary structures give opposite-signed secondary shifts between  $\text{C}^\beta$  on one hand and  $\text{C}^\alpha$  and CO on the other, the absence of opposite  $\text{C}^\alpha$  and CO shift changes from the  $\text{C}^\beta$  shift change suggests that the cause for the  $\text{C}^\beta$  change is packing interaction with amantadine rather than ( $\phi$ ,  $\psi$ ) angle changes of the S31 backbone.

To confirm the S31  $\text{C}^\beta$  chemical shift, we carried out a 1D  $\text{CH}_2$  spectral editing experiment. The ex-

periment selectively detects  $\text{CH}_2$  groups such as Ser  $\text{C}^\beta$  while suppressing the signals of all CH groups such as backbone  $\text{C}^\alpha$  atoms. Figure 4 compares the  $\text{CH}_2$ -edited spectra (Fig. 4b and d) with the  $^{13}\text{C}$  CP spectra (Fig. 4a and c) of the apo and complexed M2TMP. The unfiltered spectra contain all labeled peptide  $^{13}\text{C}$  signals as well as natural abundance lipid  $^{13}\text{C}$  signals; thus, they are less resolved than Fig. 2. The  $\text{CH}_2$  filter suppressed the V28 and L36  $\text{C}^\alpha$  signals but retained S31  $\text{C}^\beta$ , L36  $\text{C}^\beta$ , and the main lipid  $\text{CH}_2$  peaks. The method does not completely suppress the mobile  $\text{CH}_3$  groups; however, their chemical shifts do not overlap with Ser  $\text{C}^\beta$ . The  $\text{CH}_2$ -edited spectra of the apo and complexed peptide (Fig. 4b and d) confirm the 1.0-ppm upfield shift of the S31  $\text{C}^\beta$  peak upon amantadine binding.

In addition to S31, V28  $\text{C}^\alpha$  and CO show significant chemical shift changes in the 2D spectra (Fig. 3c). The CO frequency increased by 1.4 ppm while the  $\text{C}^\alpha$  chemical shift increased by 0.7 ppm (Table 1). These downfield shift changes are consistent with a more ideal helical conformation in the presence of amantadine. Moreover, the CO chemical



**Fig. 4.** Selective detection of S31  $\text{C}^\beta$  by  $\text{CH}_2$  editing. (a)  $^{13}\text{C}$  CP-MAS spectrum of apo M2TMP. (b)  $\text{CH}_2$ -edited spectrum of apo M2TMP. (c)  $^{13}\text{C}$  CP-MAS spectrum of amantadine-bound M2TMP. (d)  $\text{CH}_2$ -edited spectrum of bound M2TMP. Note the suppression of the  $\text{C}^\alpha$  CH peaks in (b) and (d).

**Table 1.**  $^{13}\text{C}$  and  $^{15}\text{N}$  chemical shifts (in parts per million) of M2TMP in DLPC bilayers at 243 K without and with amantadine (Amt)

		N	CO	C $^{\alpha}$	C $^{\beta}$	C $^{\gamma}$	C $^{\delta}$	C $^{\epsilon}$
L26	Apo	117.7	176.6	55.5	39.1	25.2	23.8	21.2
	Amt	117.5	176.3	55.7	39.4	25.2	23.3	20.9
V27	Apo	120.4	177.8	63.8	29.7	21.2	19.3	
	Amt	119.9	178.1	63.9 <sub>s</sub>	30.0	20.8	19.5	
				<b>62.0<sub>w</sub></b>				
V28	Apo	<b>122.8</b>	<b>175.9</b>	<b>64.8</b>	29.7	20.7	19.5	
	Amt	<b>125.9</b>	<b>177.0</b>	<b>65.4</b>	29.7	20.8	19.0	
A29	Apo	<b>120.9</b>	176.7	53.5	16.6			
	Amt	<b>121.7</b>	176.8	53.5	16.3			
A30	Apo	118.0 <sub>w</sub>	177.7	52.8	16.5			
		<b>119.4</b>						
	Amt	118.7	177.5	52.8	17.0			
S31	Apo	<b>114.7</b>	<b>173.7</b>	61.2	<b>60.8</b>			
	Amt	<b>121.4</b>	<b>173.1</b>	61.3	<b>59.8</b>			
I33	Apo	<b>120.3</b>	175.7	63.1	35.4	28.5	15.7	11.8
							<b>14.9</b>	
	Amt	<b>119.4</b>	176.0	63.2	35.4	28.3	16.0	12.0
G34	Apo	<b>107.1</b>	<b>173.0</b>	<b>45.7</b>				
	Amt1	<b>106.3</b>	173.2	45.5				
	Amt2	<b>109.7</b>	<b>175.0</b>	<b>45.0</b>				
I35	Apo	<b>122.3</b>	175.5	63.9	35.7	<b>28.1</b>	15.7	11.7
	Amt	<b>124.6</b>	175.4	63.8	35.8	<b>27.3</b>	15.6	11.6
L36	Apo	119.9	<b>175.8</b>	56.0	39.4	24.9	24.2	21.2
	Amt	119.6	<b>175.3</b>	55.8	39.5	24.7	23.8	21.2
L38	Apo	<b>117.8</b>	175.8	56.1	37.5 <sub>w</sub>	25.0	24.2	<b>20.1</b>
					39.5 <sub>s</sub>			
	Amt	<b>117.1</b>	175.8	56.0	37.4 <sub>m</sub>	24.9	23.9	<b>21.0</b>
					39.6 <sub>s</sub>			

Sites with chemical shift differences greater than 0.5 ppm are in boldface. Letters s, m, and w denote strong, medium, and weak, respectively. The  $^{13}\text{C}$  and  $^{15}\text{N}$  shifts are referenced to TMS and liquid  $\text{NH}_3$ , respectively.

shift is sensitive to hydrogen bonding,<sup>27</sup> thus, the larger increase of the CO chemical shift over C $^{\alpha}$  suggests that amantadine may perturb the hydrogen-bond network around V28.

#### $^{15}\text{N}$ chemical shifts of VSL-M2TMP without and with amantadine

Low-temperature 1D  $^{15}\text{N}$  MAS spectra of the apo and complexed VSL-M2TMP are shown in Fig. 5. The assignment of the  $^{15}\text{N}$  peaks is based on 2D  $^{15}\text{N}$ - $^{13}\text{C}$  correlation spectra shown in Fig. 6. Both the  $^{15}\text{N}$  chemical shifts and  $^{15}\text{N}$  linewidths show dramatic changes upon amantadine binding. The V28 and S31  $^{15}\text{N}$  peaks move downfield, and all three sites are narrowed by a factor of 2. The drug-complexed peptide has a full width at half maximum of 2.0 ppm for all three sites, while the apo peptide linewidths range from 3.5 to 5.3 ppm (Table 2).

2D  $^{15}\text{N}$ - $^{13}\text{C}$  correlation spectra are shown in Fig. 6 to provide definitive evidence of structure perturbation by amantadine. Consistent with the  $^{13}\text{C}$  data, the most pronounced  $^{15}\text{N}$  chemical shift change occurs at S31 (6.7 ppm), followed by V28, which has a more modest but still significant  $^{15}\text{N}$  shift increase of 3.1 ppm. Similar to the  $^{13}\text{C}$  data, L36 exhibits little change in its  $^{15}\text{N}$  chemical shift.

#### Chemical shift perturbation at the M2TMP core

Table 1 summarizes all  $^{13}\text{C}$  and  $^{15}\text{N}$  chemical shifts measured for 11 residues, including L26, V27, V28, A29, A30, S31, I33, G34, I35, L36, and L38. This table extends the one recently reported<sup>7</sup> by the addition of V28, S31, and L36 chemical shifts; the addition of carbonyl chemical shifts for all residues; and the more accurately measured side-chain methyl chemical shifts (S.D.C., T.M., and M.H., unpublished results). Figure 7a plots the average chemical shift change per residue due to amantadine binding:

$$\text{chemical shift perturbation} = \frac{1}{n} \sum_{i=1}^n |\delta_{\text{apo},i} - \delta_{\text{amt},i}|,$$

where  $n$  is the number of chemical shift values available in each residue. Both the  $^{13}\text{C}$  and  $^{15}\text{N}$  chemical shifts are included, and the absolute value of the chemical shift difference is summed to avoid cancellation of positive and negative shift changes. Figure 7a shows three distinct local maxima of chemical shift perturbation: S31, G34, and V28, with average chemical shift changes of 2.1, 1.1, and 0.9 ppm, respectively.

#### Conformational distributions at V28, S31, and L36

While isotropic chemical shifts report the average conformation, linewidths of frozen proteins indicate the conformational distribution. Apparent linewidths ( $\Delta^*$ ) directly read off from the spectra are indicative of conformational heterogeneity, while homogeneous linewidths ( $\Delta$ ) result from  $T_2$  relaxation, which is induced by microsecond-time scale molecular motions that modulate the nuclear spin interactions. The homogeneous linewidths can be measured using spin echo experiments and are related to  $T_2$  by  $\Delta = 1/\pi T_2$ . We extracted the  $^{15}\text{N}$  and

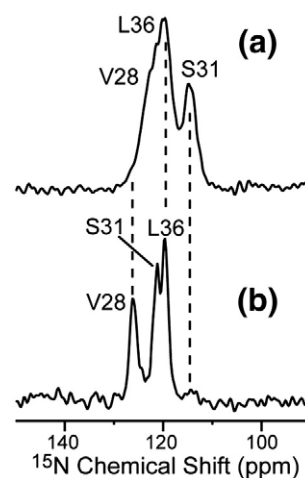


**Fig. 5.** 1D  $^{15}\text{N}$  CP-MAS spectra of VSL-M2TMP in DLPC bilayers at 243 K. (a) Without amantadine. (b) With amantadine.

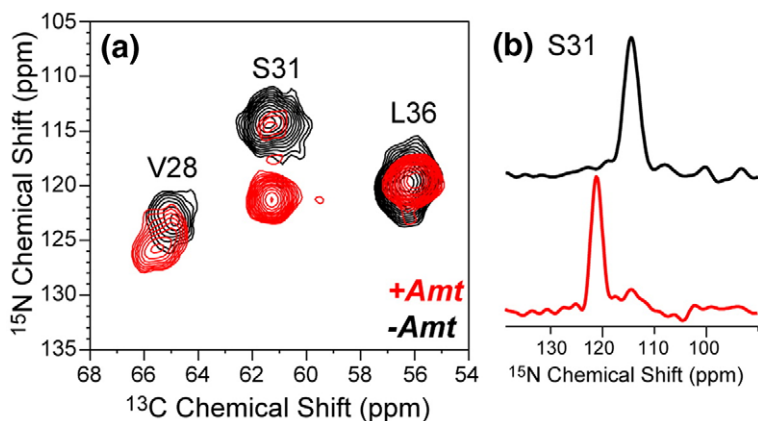


**Fig. 6.** (a) 2D  $^{15}\text{N}$ - $^{13}\text{C}$  correlation spectrum of VSL-M2TMP in DLPC bilayers at 243 K. Black: without amantadine. Red: with amantadine. (b) S31  $^{15}\text{N}$  cross sections.

$^{13}\text{C}$  apparent linewidths from 2D  $^{13}\text{C}$ - $^{13}\text{C}$  and  $^{15}\text{N}$ - $^{13}\text{C}$  correlation spectra where all signals are resolved. Low-temperature spectra are used since they capture all conformations present in the fluid membrane. Table 2 shows that the apparent linewidths of most sites in V28, S31, and L36 are similar between the apo and complexed peptide, with the exception of all amide  $^{15}\text{N}$  sites and S31  $\text{C}^\alpha$  and  $\text{C}^\beta$ .

To obtain the  $^{13}\text{C}$  homogeneous linewidths, we measured the  $T_2$  relaxation times under a  $^1\text{H}$  decoupling field of 71 kHz.  $^1\text{H}$ -decoupled heteronuclear  $T_2$  is mainly sensitive to motions on the time scale of the inverse of the decoupling field, which is thus  $\sim 10 \mu\text{s}$ . Table 2 shows that the  $^{13}\text{C}$  homogeneous linewidths are identical between the apo and complexed peptide within experimental uncertainty, indicating that all peptide motion is frozen at 243 K and does not cause different relaxation between the apo and complexed states. Thus, the narrower  $\Delta^*$  of S31 in the complexed peptide must be attributed to reduced conformational heterogeneity due to drug binding.

**Table 2.**  $^{13}\text{C}$  and  $^{15}\text{N}$  apparent ( $\Delta^*$ ) and intrinsic linewidths ( $\Delta$ ) of VSL-M2TMP at 243 K under 71 kHz  $^1\text{H}$  decoupling

Residue	Site	$\Delta^*$ , apo (ppm)	$\Delta$ , apo (ppm)	$\Delta^*$ , +Amt (ppm)	$\Delta$ , +Amt (ppm)
V28	N	<b>5.3</b>	–	<b>2.0</b>	–
	$\text{C}^\alpha$	1.4	0.60	1.3	0.60
	$\text{C}^\beta$	1.1	0.67	1.0	0.67
	$\text{C}^{\gamma 1}$	1.7	0.40	1.4	0.40
	$\text{C}^{\gamma 2}$	1.3	0.40	1.6	0.40
S31	N	<b>3.5</b>	–	<b>2.0</b>	–
	$\text{C}^\alpha$	<b>1.5</b>	0.60	<b>0.93</b>	0.60
	$\text{C}^\beta$	<b>2.8</b>	0.57	<b>1.6</b>	0.57
L36	N	<b>4.0</b>	–	<b>2.0</b>	–
	$\text{C}^\alpha$	1.0	0.47	0.9	0.47
	$\text{C}^\beta$	1.3	0.73	1.1	0.73
	$\text{C}^\gamma$	1.1	0.57	1.0	0.57
	$\text{C}^{\delta 1}$	1.9	0.40	1.7	0.40
	$\text{C}^{\delta 2}$	1.4	0.40	1.4	0.40

Significant linewidth changes between the apo and amantadine-bound samples are in boldface.

### Amantadine-induced changes of M2TMP dynamics

Complementing the low-temperature chemical shift and linewidth data, we measured the  $^{13}\text{C}$  spectra of M2TMP in the liquid-crystalline phase of the lipid bilayer to obtain information on the molecular motion of the protein. Previous data on eight other labeled residues found across the board line narrowing by amantadine at high temperature.<sup>7</sup> This is now observed at V28, S31, and L36 as well. Figure 8 shows the  $^{13}\text{C}$  CP-MAS spectra of apo and complexed VSL-M2TMP in DLPC bilayers from 243 to 313 K. At 243 K, the spectra show strong intensities characteristic of immobilized molecules for both the apo and complexed M2TMP. When the temperature increased to 283 K, near the phase transition temperature of the DLPC bilayer, the peak intensities decrease significantly for both samples, indicating intermediate-time scale motion. Increasing the temperature to the near-physiological 313 K partially recovered the intensities of both samples, but the amantadine-complexed peptide exhibits stronger CP intensities than the apo peptide, especially for methylene groups such as L36  $\text{C}^\beta$  and S31  $\text{C}^\beta$ .

To probe fluid-phase dynamics of M2TMP, we measured the  $^{13}\text{C}$   $T_2$  of the peptide at 303 K using the Hahn-echo experiment and compared them between the apo and complexed states. Table 3 shows that the  $^{13}\text{C}$   $T_2$  values increase by 1.5- to 4.0-fold upon drug binding, consistent with what was observed at other residues.<sup>7</sup> Plotting the fractional increase of the  $^{13}\text{C}$   $T_2$  for the 11 residues as

$$\text{fractional } T_2 \text{ change} = \frac{1}{n} \sum_{i=1}^n \frac{T_{2,\text{amt}}^i - T_{2,\text{apo}}^i}{T_{2,\text{amt}}^i},$$

we find two local maxima, V27 and S31 (Fig. 7b).

### Dependence of M2 structural changes on amantadine concentration and specificity of the structure changes

The above amantadine-induced chemical shift changes were measured on membrane samples pre-

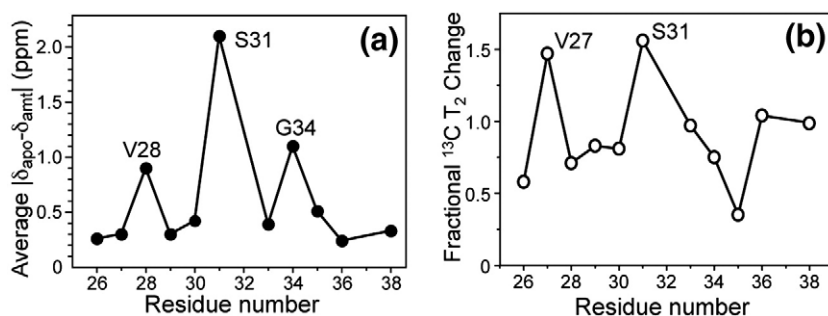


**Fig. 7.** Amantadine-induced changes of M2TMP structure and dynamics in DLPC bilayers. (a) Average isotropic chemical shift changes for each residue, measured at low temperature. (b) Average  $^{13}\text{C}$   $T_2$  changes, measured at 303 K.

pared from buffers containing 10 mM amantadine.  $^1\text{H}$  solution NMR analysis of the supernatant after the membrane is pelleted showed that the amount of amantadine bound to the membrane typically corresponded to an M2:amantadine molar ratio of  $\sim 1:10$ . This is well in excess of the expected stoichiometric M2:amantadine ratio, which is either 4:1 based on the crystal structure or 1:1 based on the solution NMR structure. The use of excess amantadine is largely due to the concern that the lipophilic drug, which readily partitions into the lipid membrane from the aqueous solution,<sup>28–30</sup> may not all end up in the channel. Nevertheless, the question arises as to whether the observed M2 chemical shift changes result from nonspecific effects of amantadine on the lipid bilayer that then indirectly change the peptide structure or whether it is due to direct amantadine–peptide interactions. To address this question, we prepared a VSL-M2TMP sample in DLPC bilayers with a much lower M2:amantadine molar ratio of 1:2, by directly titrating a quantitative amount of amantadine solution into the M2 membrane pellet. The resulting 2D spectrum (Fig. 9c) shows that 70% of the S31  $^{15}\text{N}$ – $^{13}\text{C}^\alpha$  peak has shifted to the bound position. The 30% remaining unshifted signal can be attributed to channels without amantadine, implying that some amantadine is dispersed in the rest of the lipid bilayer. The observation of the same chemical shift perturbation at much lower amantadine levels confirms that the structural changes we detect at high concentration result from

direct drug–protein interactions rather than non-specific lipid-mediated effects.

A related question is whether amantadine causes the M2  $^{13}\text{C}$   $T_2$  relaxation time changes (Fig. 7b) by indirect and nonspecific changes of the membrane dynamics. To answer this question, we prepared two DLPC samples without the M2 peptide. One sample does not contain amantadine and the other contains 10 mM amantadine in the buffer during vesicle formation. The  $^{13}\text{C}$   $T_2$  relaxation times of the two DLPC samples were measured at 313 K by direct polarization Hahn-echo experiments, in which identical  $^1\text{H}$  decoupling field strengths (30 kHz) were used to ensure that the motion is probed on the same time scale. Figure 10 shows the fractional  $T_2$  changes for all resolved DLPC carbon sites. It can be seen that all sites except the head-group  $\text{C}^\beta$  experience negligible  $T_2$  changes of less than  $\pm 10\%$  upon amantadine binding. Moreover, most DLPC sites show a decrease of  $^{13}\text{C}$   $T_2$ , opposite to the trend for M2TMP. Thus, amantadine does not significantly impact the lipid dynamics, and the dynamic changes of M2TMP are specifically due to peptide–drug interactions.

## Discussion

The goals of this study are twofold: obtain a chemical-shift-constrained backbone structure of M2TMP in the absence and presence of amantadine

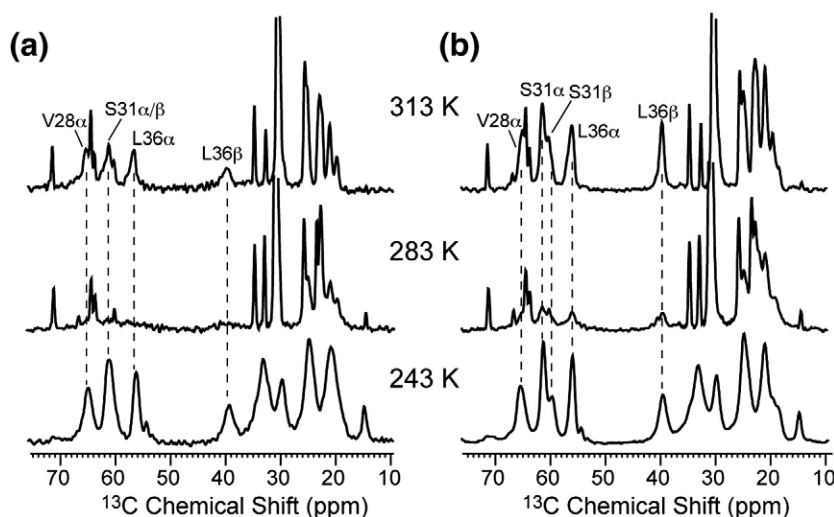


**Fig. 8.**  $1\text{D } ^{13}\text{C}$  variable-temperature CP-MAS spectra of VSL-M2TMP bound to DLPC bilayers. (a) Without amantadine. (b) With amantadine. Temperatures from top to bottom are 313, 283, and 243 K.



**Table 3.**  $^{13}\text{C}$  homogeneous  $T_2$  (in milliseconds) of VSL-M2TMP at 303 K with 71 kHz  $^1\text{H}$  decoupling

Residue	Site	$T_2$ , apo	$T_2$ , +Amt
V28	$\text{C}^\alpha$	1.0	2.5
	$\text{C}^{\gamma 1}$	3.0	5.6
	$\text{C}^{\gamma 2}$	2.6	4.7
S31	$\text{C}^\alpha$	1.1	3.5
	$\text{C}^\beta$		3.8
L36	$\text{C}^\alpha$	1.0	3.6
	$\text{C}^\beta$	1.1	3.5
	$\text{C}^\gamma$	2.6	7.9
	$\text{C}^{\delta 1}$	6.0	11.6
	$\text{C}^{\delta 2}$	6.0	–

and determine the size and nature of the drug-induced conformational change, particularly at Ser31. With the consolidation of the  $^{13}\text{C}$  and  $^{15}\text{N}$  chemical shifts for 11 consecutive residues in the core of the peptide, we can now use the TALOS program to predict the backbone torsion angles of the M2 peptide in the lipid bilayer.

### Backbone structure of M2TMP monomer

The TALOS-predicted ( $\phi$ ,  $\psi$ ) torsion angles of M2TMP based on the  $^{13}\text{C}$  and  $^{15}\text{N}$  chemical shifts are shown in Fig. 11 and tabulated in [Supplementary Table S1](#). TALOS requires the chemical shifts of three consecutive residues to predict the torsion angles of the central residue. Since I32 and H37 have not been labeled in our studies but data for their neighboring residues are available, we used database ideal helical chemical shifts for these two residues as placeholders in order to extract the ( $\phi$ ,  $\psi$ ) angles of their neighboring residues. The torsion angles of I32 and H37 are thus not entirely constrained (shaded points in Fig. 11).

The chemical shift changes listed in Table 1 indicate a number of ( $\phi$ ,  $\psi$ ) changes, although none of them are large enough to alter the basic helical nature of the protein. The first region of change is V27–V28 and the second is A30–S31. Interestingly, while the chemical shifts of V27 and A30 themselves are not significantly perturbed, the larger chemical shift changes of their C-terminal residues, V28 and S31, translated into significant ( $\phi$ ,  $\psi$ ) changes at V27 and A30. In particular, the large  $^{15}\text{N}$  chemical shift changes of S31 and V28 indicate that the  $\psi$  angle of A30 and V27, respectively, are significantly perturbed.

The G34–I35 pair is the third region of ( $\phi$ ,  $\psi$ ) perturbation that merits attention. Not only do both residues show clear chemical shift perturbations, but also two sets of G34  $^{15}\text{N}$  and  $^{13}\text{C}$  chemical shifts are present in the complexed peptide (Table 1). We denote the set with an upfield  $^{15}\text{N}$  shift of 106.3 ppm as amt1 and the set with a downfield  $^{15}\text{N}$  chemical shift of 109.7 ppm as amt2. The amt1 chemical shifts are similar to the apo values, suggesting that a population of peptide either does not bind or only weakly binds amantadine. In contrast, the amt2 chemical shifts are significantly different from the

apo values and cause larger G34  $\phi$  and I35  $\psi$  changes (Fig. 11). Overall, the TALOS-predicted ( $\phi$ ,  $\psi$ ) angle differences between the apo and amt2 forms of M2TMP are on average ( $1.8^\circ$ ,  $2.8^\circ$ ).

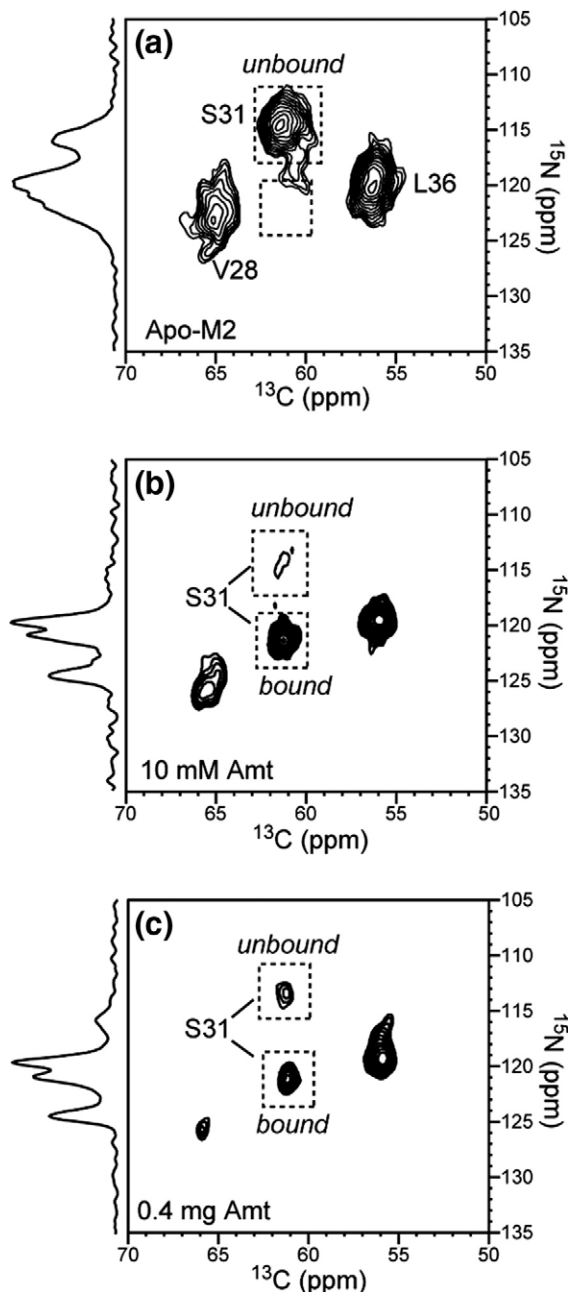


**Fig. 9.** 2D  $^{15}\text{N}$ – $^{13}\text{C}$  correlation spectra of VSL-M2TMP in DLPC bilayers with different amounts of amantadine. The S31  $^{15}\text{N}$ – $^{13}\text{C}^\alpha$  cross peak is used to indicate the degree of amantadine binding. 1D  $^{15}\text{N}$  CP spectra are shown projected from the indirect dimension of each spectrum. (a) No amantadine. The S31 peak is completely in the unbound position. (b) Amantadine added at 10 mM in the buffer. The M2:amantadine molar ratio in the final membrane is  $\sim 1:8$ . Almost all S31 intensities are at the bound position. (c) Amantadine directly titrated into the membrane pellet. The M2:amantadine molar ratio in the final pellet is  $\sim 1:2$ . Seventy percent of the S31 intensity is at the bound position.

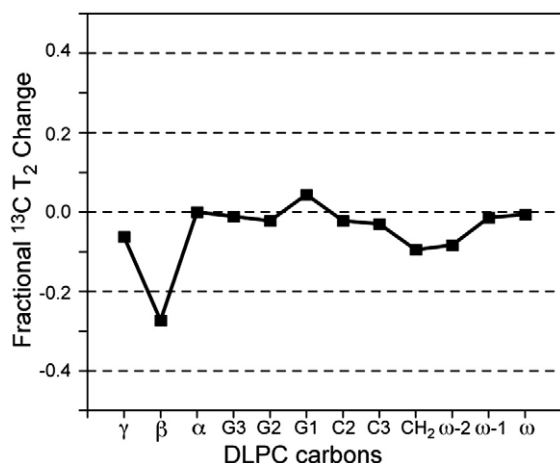


**Fig. 10.** Fractional  $^{13}\text{C}$   $T_2$  changes of DLPC lipid carbons upon amantadine binding at 313 K. No M2 peptide is present. The fractional change is calculated as  $(T_{2,\text{amt}} - T_{2,\text{apo}})/T_{2,\text{apo}}$ .

Figure 12 shows the monomer structure of the M2TMP backbone based on the TALOS ( $\phi$ ,  $\psi$ ) angles. The apo structure is shown in black and gray and the amt2 structure is shown in blue and cyan. For residues 39 down to the end of the helix, where no experimental chemical shifts are available, we used the helical torsion angles of  $(-59^\circ, -44^\circ)$  for both the apo and complexed peptide. Figure 12 shows that both helices are relatively ideal. The side views of the two models are oriented such that the N-terminus half of the helix above G34 has a tilt angle of  $35^\circ$  for the apo peptide and  $38^\circ$  for the amantadine-bound peptide. These tilt angles were

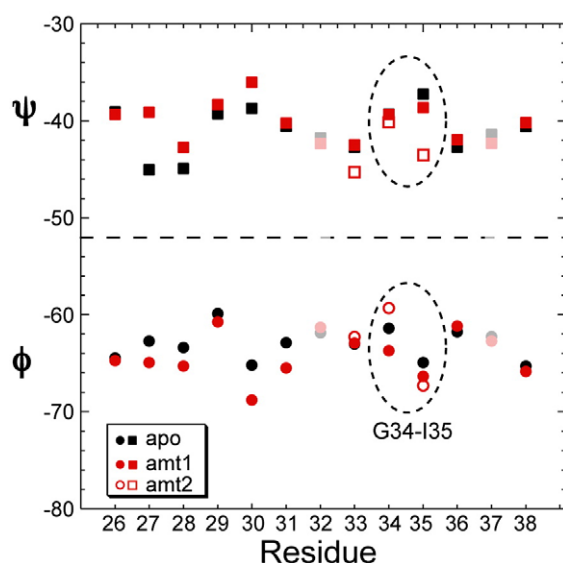


**Fig. 11.** TALOS-predicted ( $\phi$ ,  $\psi$ ) angles for residues 26–38 of apo (black) and amantadine-complexed M2TMP (red). Filled and open red symbols denote the conformations of amt1 and amt2, which differ at G34. Residues 32 and 37 are shaded due to incomplete experimental data.

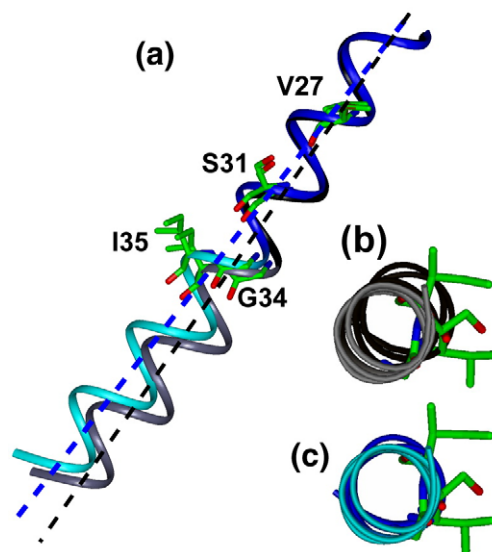


**Fig. 12.** Chemical-shift-constrained backbone structure of the M2TMP monomer. Apo: black and gray ribbon. Amantadine-bound: blue and cyan ribbon. (a) Side view of the helix with tilt angles determined by SSNMR. (b) Top view of the apo monomer. (c) Top view of the amantadine-complexed monomer. The apo peptide has a more noticeable kink.

measured on hydrated vesicle samples by  $^{15}\text{N}$  NMR.<sup>7,20,21</sup> When the N-terminal segments of the two helices are superimposed, it becomes apparent that the amt2 and apo helices diverge in the orientation of the segment C-terminal to G34. Comparing the helical axis for residues 27–33 with the helical axis for residues 35–41, we find a kink of  $8^\circ$  for the apo peptide and  $5^\circ$  for the amt2 helix. The helical axis orientations were calculated as the average N–H vector orientation of each seven-residue segment, which approximately complete two turns of the helix.

$^{15}\text{N}$  chemical shift anisotropies and N–H dipolar couplings have been measured on M2TMP in glass-plate-aligned DMPC/DMPG membranes using static NMR techniques. These data indicated a pronounced helix kink of  $13^\circ$  for the drug-complexed M2TMP.<sup>18</sup> The site of the kink is G34, in good qualitative agreement with the current chemical shift data that indicate structure perturbation at G34–I35. However, the kink from the oriented-sample NMR data is much larger than that deduced from the current unoriented MAS samples. While static  $^{15}\text{N}$  anisotropic couplings are very sensitive to helix orientations, it is possible that glass-plate samples may exert additional influences on the protein orientation through mechanical stress and hydration. In comparison, the unoriented vesicle samples should place much less stress on membrane proteins and thus provide a useful check of the protein orientation. Moreover, the membrane thickness may affect the helical kink. The aligned membrane experiments were done in DMPC and 1,2-dimyristoyl-*sn*-glycero-3-phosphatidyl-glycerol (DMPG)

lipids while the current experiments were conducted in the thinner DLPC bilayers.

The recent solution NMR<sup>14</sup> and X-ray structures<sup>15</sup> of drug-bound and detergent-solubilized M2 peptide show different kinks of the helical backbone. Comparing the same segments of 27–33 and 35–41, the solution NMR structure [Protein Data Bank (PDB) code: 2RLF] has a minor kink of 4°, while the refined crystal structure (PDB code: 3C9J) has a larger kink of 12°. Thus, the amt2 kink of 5° measured by MAS-SSNMR falls within the range of reported by all methods.

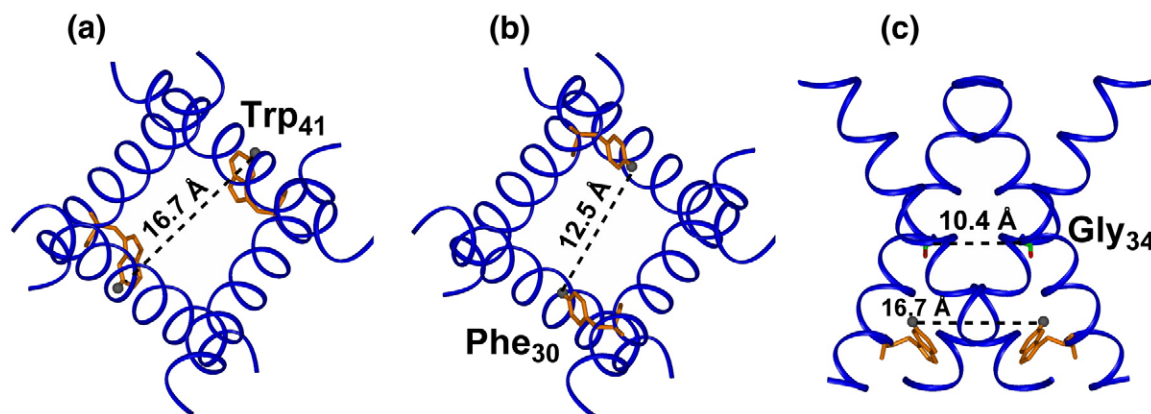
Paradoxically, the structure of the apo M2 peptide is much less known than that of the drug-bound M2. Static <sup>15</sup>N NMR data of the apo peptide suffered from broad linewidths due to unfavorable conformational dynamics of the protein,<sup>19,31</sup> which made it difficult to detect possible helix orientation differences between the N- and C-terminal segments of the helix. The MAS-NMR approach here bypasses this difficulty since its main structural constraints are isotropic chemical shifts, which can be measured at low temperature where motion is frozen. Based on the <sup>13</sup>C and <sup>15</sup>N isotropic chemical shifts, the helical backbone of the apo M2TMP is also not straight but has a kink of ~9°, as shown in the top view in Fig. 12b. While the chemical-shift-constrained backbone conformations are only indirect constraints of the helix orientation, the data nevertheless suggest that the presence of Gly34 in the peptide may cause a small kink already in the apo protein. This would not be surprising since Gly is a helix breaker in globular proteins.<sup>32</sup> In membrane proteins, Gly adheres to more ideal helical torsion angles,<sup>33</sup> as in the case of Gly34, but a small deviation from ideality is all that is required to cause a small kink of the helical axis. If confirmed, then the role of helix kink to the M2 channel activity would need to be considered. Since Gly34 is located roughly one turn away from His37, which is responsible for proton conduction, we speculate that the kink may be required for establishing the proper His37 side-chain conformation. The change in the

helix kink after amantadine binding may thus be relevant for proton blockage.

### Backbone structure of the M2 tetramer

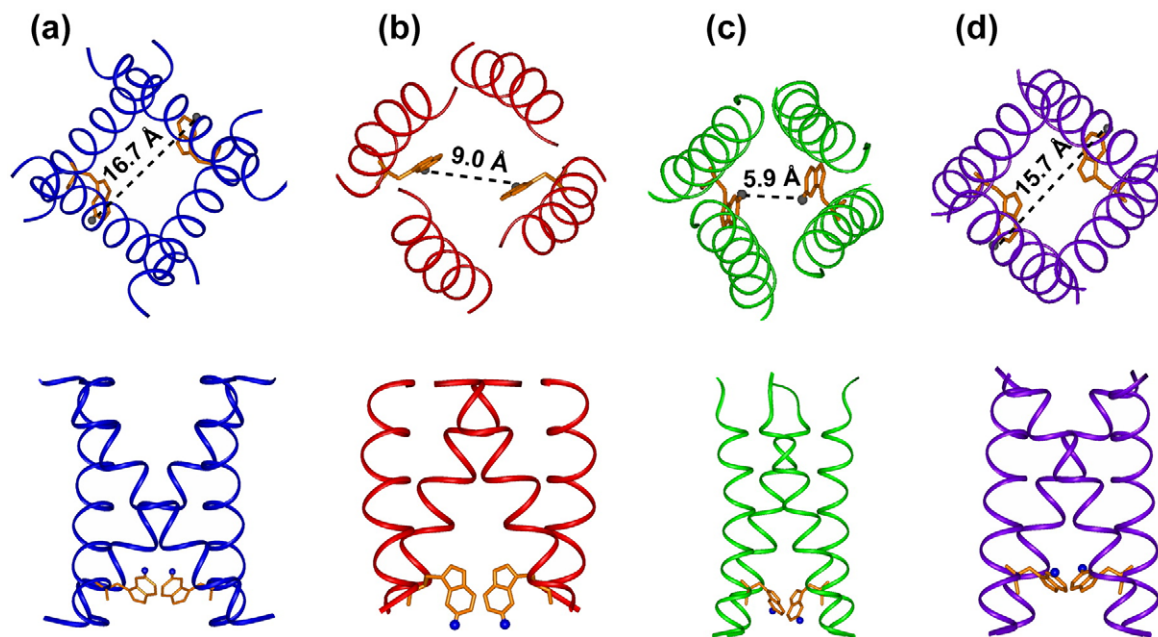
Based on the chemical-shift-constrained monomer structure, we now construct a tetramer model of amantadine-bound M2TMP using the measured helix orientation and interhelical distances. Again, the helix tilt angle is set to be 35° for the apo peptide<sup>20</sup> and 38° for the amantadine-bound peptide<sup>7,21</sup> for the segment N-terminal to Gly34. We have previously measured two <sup>19</sup>F–<sup>19</sup>F interhelical distances at Trp41 5-<sup>19</sup>F<sup>23</sup> and Phe30 4-<sup>19</sup>F<sup>22,34</sup> using <sup>19</sup>F spin diffusion NMR.<sup>35</sup> By design, these experiments measure all three distances in the symmetric tetramer, including two nearest neighbor  $i-i\pm1$  distances  $r_{nn}$  and the diagonal  $i-i+2$  distance,  $\sqrt{2}r_{nn}$ . The tetrameric nature of the channel is directly confirmed in the experiment as an equilibrium value of 1/4. We found an  $r_{nn}$  of 11.8 Å for Trp41 5-<sup>19</sup>F and 8.5 Å at Phe30 4-<sup>19</sup>F. The former constrained the Trp41 side-chain rotamer to  $t_{90}$  ( $\chi_1=180^\circ$ ,  $\chi_2=90^\circ$ ), while the latter constrained the Phe30 rotamer to  $t$  ( $\chi_1=180^\circ$ ). In addition to these two interhelical distances, we used a Gly34 C $\alpha$ –C $\alpha$  diagonal distance of 10.4 Å<sup>36</sup> in building the tetramer model.

Figure 13 shows the tetramer model for the amt2 peptide where the three distance restraints are indicated. For clarity, we show only the diagonal distances, which are 16.7, 12.5, and 10.4 Å for Trp41 5-<sup>19</sup>F, Phe30 4-<sup>19</sup>F, and Gly34 C $\alpha$ , respectively. For comparison, the tetramer structure solved by <sup>15</sup>N static NMR (PDB code: 2H95), solution NMR (PDB code: 2RLF), and X-ray crystallography (PDB code: 3C9J) is shown in Fig. 14b–d. A number of differences can be seen. First, both the solution NMR structure in DHPC micelles and the static <sup>15</sup>N NMR structure in DMPC bilayers give interhelical Trp41 distances that are much shorter than the measured value. This discrepancy is mainly due to the different ( $\chi_1$ ,  $\chi_2$ ) angles in these models:  $t_{90}$  in the solution NMR structure and (–95°, 125°) in the static <sup>15</sup>N



**Fig. 13.** Tetramer model of M2TMP constrained by SSNMR chemical shifts, interhelical distances, and helix orientations. (a) Trp41 5-<sup>19</sup>F distance between the two opposite helices is 16.7 Å.<sup>23</sup> (b) Phe30 4-<sup>19</sup>F diagonal distance is 12.5 Å.<sup>22</sup> (c) Side view of the tetramer, with a diagonal Gly34 C $\alpha$ –C $\alpha$  distance of 10.4 Å.





**Fig. 14.** Comparison of the MAS-NMR structure model with other recently published structures of drug-complexed M2. The Trp41 indole ring and the diagonal distance between its 5- $^{19}\text{F}$  or  $\text{H}^{53}$  are indicated. (a) MAS-NMR model of amantadine-bound M2TMP. (a)  $^{15}\text{N}$  static SSNMR model of amantadine-bound M2TMP (PDB code: 2H95). (b) Solution NMR structure of rimantadine-bound M2(18–60) (PDB code: 2RLF). (c) Crystal structure of amantadine-bound M2TMP (PDB code: 3C9J).

NMR model. The crystal structure has the  $t_{90}$  rotamer for Trp41 and thus gives consistent interhelical distances with the  $^{19}\text{F}$  MAS-NMR result. Second, the MAS-SSNMR tetramer model is more open at the N-terminus than the solution NMR and crystal structures. At Val27, the  $\text{H}^{\gamma}$ – $\text{H}^{\gamma}$  diagonal distances in our model are  $\sim 11$  Å but are 5–7 Å in the other models. The relatively large pore opening at Val27 in our model is a direct result of the helix orientation and is consistent with the small chemical shift perturbation of Val27 and the interhelical Phe30 distance constraint. This large opening may be necessary to allow the drug to bind at the N-terminus. The smaller Val27 constriction in the solution NMR and crystal structures is a direct result of smaller tilt angles, which may be influenced by the detergent matrix used. It is well documented that the orientation of the M2 transmembrane helix is relatively plastic, readily affected by the bilayer thickness.<sup>20,37</sup> In DLPC and DMPC bilayers, both MAS and static NMR experiments point to a large helical tilt angle of about  $35^\circ$ , while in POPC bilayers, the tilt angle is only  $26^\circ$ .<sup>20</sup>

In contrast to the openness of the channel at Val27, the MAS-derived structural model shows a tight Ser31 constriction, with a distance of 9.0 Å between the two opposing hydroxyl oxygens. This Ser31 constriction is similar to the crystal structure but tighter than the static  $^{15}\text{N}$  NMR model (11.9 Å) and the solution NMR structure (19.4 Å) (Fig. 14). Overall, the small Ser31 constriction is consistent with the large chemical shift perturbation at this site (see next section).

To compare the various M2 PDB structures with the current MAS-based model more quanti-

tatively, we used the SHIFTX program<sup>38</sup> to calculate the  $^{15}\text{N}$ ,  $^{13}\text{CO}$ ,  $^{13}\text{C}^{\alpha}$  and  $^{13}\text{C}^{\beta}$  chemical shifts for the crystal structure (PDB code: 3C9J), the solution NMR structure (PDB code: 2RLF), and the oriented SSNMR structure (PDB code: 2H95). The root-mean-square (RMS) deviations of the predicted chemical shifts from the measured values for both the apo and amantadine-bound M2TMP are summarized in [Supplementary Table S2](#). Three observations can be made. First, with the exception of the  $^{13}\text{CO}$  shifts for the oriented NMR structure model, most  $^{13}\text{C}$  RMS shift differences are in the range of 0.8–1.3 ppm, which are comparable to the standard RMS errors of the SHIFTX program. This suggests that the deviations are mostly due to systematic uncertainties in the prediction protocol rather than large secondary-structure differences. Second, the  $^{15}\text{N}$  chemical shift differences are comparable to the standard RMS error when the predicted values are compared to the measured apo chemical shifts, but the differences become almost two times larger when the predicted values are compared to the amantadine-bound chemical shifts. This further indicates the sensitivity of  $^{15}\text{N}$  chemical shifts to long-range electrostatic effects due to ligand binding and helix packing, which are not taken into account in such chemical shift prediction programs. Third, among the three PDB structures, the oriented SSNMR structure (2H95) has the largest  $^{13}\text{C}$  chemical shift deviations from the current data but the smallest  $^{15}\text{N}$  chemical shift deviations. This is consistent with the sole use of  $^{15}\text{N}$  NMR inputs to constrain the 2H95 model.



### Ser31 interaction with amantadine

The chemical shift perturbation plot (Fig. 7a) indicates maximal drug-induced changes at Ser31 and Val28, which are mainly due to the large  $^{15}\text{N}$  chemical shift changes of these two residues. Many factors influence  $^{15}\text{N}$  chemical shielding: in addition to  $(\phi, \psi, \chi)$  torsion angles,<sup>39</sup> solvation effects and electrostatic field effects can be significant. Hydrogen bonding of the NH group can cause a deshielding of as much as 13 ppm,<sup>40</sup> and  $\gamma$ -gauche effect through the side-chain torsion angle also affects the  $^{15}\text{N}$  chemical shifts.<sup>39</sup> However, database  $^{15}\text{N}$  secondary shifts show only small deviations of  $\sim 1$  ppm for the helical conformation from the random-coil values.<sup>41</sup> Thus, it is difficult to directly interpret the large  $^{15}\text{N}$  chemical shift perturbation of Ser31. Nevertheless, it is noteworthy that both the  $^{15}\text{N}$  and  $\text{C}^\beta$  chemical shifts of Ser31 in the bound peptide (Table 1) are well beyond the typical values for  $\alpha$ -helical Ser,<sup>41</sup> which are 114.9 and 61.2 ppm, respectively, while the apo peptide's Ser31 chemical shifts are within the database range for  $\alpha$ -helical Ser. This suggests that Ser31 is locally perturbed by amantadine through packing effects.

Early neutron diffraction<sup>25</sup> and MD simulations<sup>24</sup> both supported the N-terminus of the helical bundle to be the amantadine binding site. However, the recently published high-resolution crystal structure<sup>15</sup> and solution NMR structure<sup>14</sup> of M2 gave contradictory results on the drug binding site. The former shows an N-terminus binding site deeper than Ser31, while the latter puts four rimantadine molecules per channel on the C-terminus side at helical interfaces. Since then, a functional study of the proton conductivity of M2 mutants has been carried out, which supports the N-terminus region as the primary amantadine binding site with channel inhibition properties.<sup>42</sup>

While the current data do not directly probe the drug binding site, several indirect pieces of structural evidence support an N-terminus location for amantadine. First, Ser31 is the only residue among the three studied here whose side-chain  $\text{C}^\beta$  line-width is reduced. This may reflect side-chain conformational ordering necessary to form the appro-

priate hydrogen bond with amantadine. Second, the chemical shift perturbation for the segment N-terminal to G34 is extensive (Fig. 11), with only the lipid-facing A29 and the very upstream L26 showing no torsion angle changes. Third, both V28 and L36 lie at lipid-facing positions (*b* and *c*) of the heptad repeat, but the chemical shift perturbation of the N-terminus V28 is much larger than that of the C-terminus L36.

Assuming that amantadine indeed binds the N-terminus portion of the channel, we can model the distances of amantadine from Ser31 in the tetramer (Fig. 15). Using the height of amantadine found in the crystal structure as a template, we found that if the amine points to the center of the membrane, then the  $R_{\text{NO}}$  distances between Ser31 OH and amantadine  $\text{NH}_2$  are 7.5–8.0 Å, too long for hydrogen bonding. However, if the amine points to the membrane surface, then much shorter  $R_{\text{NO}}$  distances of  $\sim 4.5$  Å are found. This amine-up orientation is supported by a recent paramagnetic relaxation NMR and MD simulation study of the depth of insertion of amantadine in the absence of M2.<sup>29</sup> The Ser31  $\chi_1$  torsion angle would need to be changed to decrease the  $R_{\text{NO}}$  distance further to form hydrogen bonds of 2.5–3.5 Å. Due to the small side chain, Ser does not have a single dominant  $\chi_1$  rotamer. For  $\alpha$ -helical backbones, the most popular rotamer of *m* ( $\chi_1 = -65^\circ$ ) is 44% while the least popular rotamer *t* ( $\chi_1 = -170^\circ$ ) still has a significant presence of 22%.<sup>43</sup> In our model (Fig. 15), both the *m* and *t* rotamers give an  $R_{\text{NO}}$  distance of  $\sim 4.5$  Å, but shorter distances of  $\sim 3.5$  Å may be reached for less canonical  $\chi_1$  angles. Ultimately, intermolecular distance experiments are necessary to test this Ser31 binding site hypothesis and to determine the high-resolution structure of the amantadine binding pocket in the bilayer-bound M2.

### MD of M2TMP

The conformational plasticity of the M2 peptide in lipid membranes is now well documented.<sup>20,31,37</sup> The low  $^{13}\text{C}$  CP intensities and short  $^{13}\text{C}$   $T_2$  relaxation times for V28, S31, and L36 at high temperature all confirm the presence of intermediate-

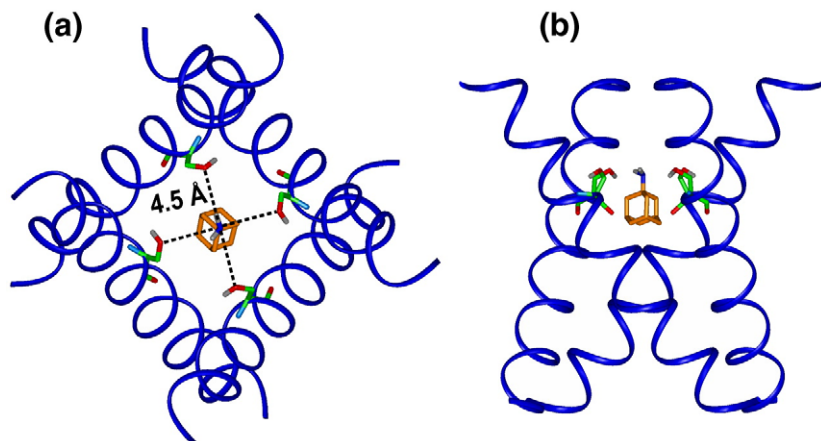


**Fig. 15.** MAS-NMR M2 tetramer model with the proposed amantadine-binding site. The height of amantadine is set to be similar to that of the crystal structure. Ser31 side-chain O distances to the amine are indicated. The top view looks down the helix axis from the N- to the C-terminus.

time scale conformational dynamics, which interfere with  $^1\text{H}$  decoupling and the  $^1\text{H}$ – $^{13}\text{C}$  cross-polarization process. In the gel phase, the motion is largely frozen; thus, the distribution of conformations sampled at high temperature is shown as isotropic chemical shift distributions. The larger low-temperature linewidths of the apo peptide compared to the complexed peptides, mostly at  $^{15}\text{N}$  sites, indicate larger conformational disorder of the apo peptide.

The nature of the M2 motion is complex. We have shown that the whole helical bundle undergoes uniaxial rotation around the bilayer normal,<sup>20</sup> which explains the observation that the short  $^{13}\text{C}$   $T_2$  times are not local but occur throughout the peptide. The lengthening of the  $T_2$  upon amantadine binding (Table 3) can, in principle, result from either a decrease or increase of motional correlation times. Temperature-sensitive relaxation times (unpublished data) indicate that the rate of motion is accelerated rather than slowed down by amantadine. Figure 7b indicates that most residues have similar amantadine-induced  $T_2$  increases except for Ser31 and Val27, whose  $T_2$  increases are much larger. We hypothesize that the exceptionally long  $^{13}\text{C}$   $T_2$  at these two sites may be caused by strong interaction with amantadine. However, the exact nature of the site-specific conformational dynamics or ordering will require further investigation.

In summary, the SSNMR chemical shifts and dynamic constraints measured here for Ser31 and other residues combine with previous data to allow the determination of a bilayer-bound structure of the transmembrane domain of this important influenza proton channel. We found that the apo and amantadine-complexed M2TMP differ in conformation mainly at three regions, V27–V28, A30–S31, and G34–I35. In particular, G34 is the site of a helical kink in both the apo and drug-bound peptide. Interhelical distances and helix orientations constrain the tetramer to be relatively open at the N-terminus, which allows the drug to enter, but tight at Ser31, which suggests hydrogen bonding between the hydroxyl group and the amantadine amine. At Trp41, the channel has an interhelical distance of  $\sim 16.7$  Å between opposing helices. Among all residues, Ser31 shows the largest drug-induced perturbations of chemical shifts, conformational dynamics, and conformational disorder, strongly suggesting that this residue is the amantadine binding site.

## Materials and Methods

### Peptides and lipids

Fmoc-protected, uniformly  $^{13}\text{C}$ ,  $^{15}\text{N}$ -labeled Val, Ser, and Leu were either prepared in-house<sup>44</sup> or purchased from Sigma-Aldrich and Cambridge Isotope Laboratories. The M2 transmembrane domain of the Udorn strain (residues 22–46)<sup>45</sup> was synthesized by PrimmBiotech (Cambridge, MA) and purified to >95% purity. The

amino acid sequence is SSDPL VVAASII GILHLIL WILDRL. The main peptide used in this work includes labeled residues at V28, S31, and L36 and is denoted VSL-M2TMP. Two previously studied M2TMP samples were also reexamined for their chemical shift assignment. One peptide contains labeled residues at L26, A29, G34, and I35, and the other peptide contains labeled sites at V27, A30, I33, and L38.

### Membrane sample preparation

M2TMP was reconstituted into DLPC bilayers by detergent dialysis.<sup>23</sup> DLPC was chosen because of the favorable dynamics of the protein in this membrane<sup>20</sup> and the similar phase transition temperature ( $-2^\circ\text{C}$ ) of this bilayer to biological cell membranes. The lipid vesicle solution was prepared by suspending dry DLPC powder (Avanti Polar Lipids) in 1 mL phosphate buffer (10 mM  $\text{Na}_2\text{HPO}_4/\text{NaH}_2\text{PO}_4$ , 1 mM ethylenediaminetetraacetic acid, and 0.1 mM  $\text{NaN}_3$ ) at pH7.5, vortexing, and freeze-thawing six to eight times to create uniform vesicles.<sup>46</sup> M2TMP powder was codissolved with OG in 2 mL phosphate buffer to an OG concentration of 30 mg/mL. The M2TMP/OG solution was mixed with an equal volume of DLPC vesicles to halve the OG concentration to 15 mg/mL. The final peptide/lipid molar ratio was 1:15. The mixture was vortexed for 1 h, allowed to stand for 6–8 h at room temperature, and then dialyzed with a 5-kDa cutoff against 1 L phosphate buffer at  $4^\circ\text{C}$  for 3 days. The buffer was changed every 8–12 h to ensure complete removal of the detergent. The dialyzed M2TMP/DLPC solution was centrifuged at  $150,000 g$  for 3 h at  $10^\circ\text{C}$ , resulting in a pellet containing  $\sim 50$  wt% water. For most amantadine-bound samples, 10 mM amantadine hydrochloride was added to the phosphate buffer either throughout the vesicle formation and peptide reconstitution processes or before ultracentrifugation. After ultracentrifugation, the percentage of amantadine left in the supernatant was quantified by  $^1\text{H}$  solution NMR and found to be roughly 60%. This gave a peptide:lipid:drug molar ratio of about 1:15:8. All membrane-bound M2 samples were thus studied at pH7.5, corresponding to the closed state of the channel.

### SSNMR spectroscopy

Most SSNMR experiments were carried out on a Bruker AVANCE-600 (14.1 T) spectrometer (Karlsruhe, Germany) using a 4-mm triple-resonance MAS probe.  $^{13}\text{C}$ – $^{13}\text{C}$  and  $^{15}\text{N}$ – $^{13}\text{C}$  2D correlation experiments were conducted at 243 K to freeze peptide motion.  $^{13}\text{C}$   $T_2$  relaxation times were measured at 303 K where the peptide is uniaxially mobile in the liquid-crystalline DLPC bilayer. Typical radiofrequency pulse lengths were 5  $\mu\text{s}$  for  $^{13}\text{C}$  and 3.5–4.0  $\mu\text{s}$  for  $^1\text{H}$ .  $^1\text{H}$  TPPM<sup>47</sup> or SPINAL<sup>48</sup> decoupling field strengths of 60–70 kHz were applied.  $^{13}\text{C}$  chemical shifts were referenced to the  $\alpha$ -Gly  $\text{C}'$  signal at 176.49 ppm on the TMS scale, and  $^{15}\text{N}$  chemical shifts were referenced to the  $^{15}\text{N}$  signal of *N*-acetyl-valine at 122.0 ppm on the liquid ammonia scale.

Three types of 2D  $^{13}\text{C}$ – $^{13}\text{C}$  correlation experiments were carried out to assign all regions of the  $^{13}\text{C}$  spectra. A DQF COSY experiment was used to obtain lipid-free protein spectra. Double-quantum filtration was performed using the dipolar recoupling sequence SPC5<sup>49</sup> with the sample spun at 7000 Hz. To better assign the carbonyl peaks, which are weak in the DQF COSY spectrum due to their large chemical shift difference from the aliphatic carbons,

we carried out a 2D  $^1\text{H}$ -driven  $^{13}\text{C}$  spin diffusion experiment with a 10-ms DARR mixing period<sup>50</sup> under 5333 Hz MAS. Finally, to completely resolve the side-chain methyl  $^{13}\text{C}$  signals, we used a double-quantum–single-quantum correlation experiment, INADEQUATE,<sup>51,52</sup> in which the SPC5 sequence was again used for double-quantum excitation and reconversion.

Heteronuclear 2D  $^{15}\text{N}$ – $^{13}\text{C}$  correlation experiments were carried out in an out-and-back fashion using the REDOR sequence<sup>53</sup> for  $^{13}\text{C}$ – $^{15}\text{N}$  coherence transfer.<sup>54</sup> The C–N recoupling times varied between 0.7 and 2.1 ms to observe one-bond *versus* multiple-bond cross peaks.

To selectively detect the S31  $\text{C}^\beta$  signal that overlaps with its  $\text{C}^\alpha$ , we carried out a methylene spectral editing experiment<sup>55</sup> at 233 K. The  $\beta$  pulse in the sequence that was responsible for clean suppression of the methine CH signals was optimized to be 40°. For MREV-8<sup>56</sup>  $^1\text{H}$  homonuclear decoupling, a  $^1\text{H}$  pulse flip angle of 94° was used.

### Structure modeling

The M2TMP tetramer structure was modeled in Insight II (Accelrys, Inc., San Diego, CA). The central segment of residues 26–38 was constrained by the chemical shifts and interhelical distances except for residues I32 and H37. The final tetramer model used the wild-type residue Ala at position 30, after the mutation Phe30 was checked for interhelical distance restraint. The atomic coordinates of the tetrameric helical bundle have been deposited in the PDB (accession number: 2kad). The SSNMR chemical shift restraints have been deposited in the Biological Magnetic Resonance Bank (accession number: 16020). These data will be released upon publication.

### Acknowledgements

This work was funded by National Science Foundation grants MCB-0543473 to M.H. and DBI-0421374 for the 600-MHz NMR spectrometer. The authors thank Professor Bill DeGrado for discussions and sharing the refined crystal structure coordinates and Professor Klaus Schmidt-Rohr for providing the pulse sequence for the  $\text{CH}_2$  selection experiment.

### Supplementary Data

Supplementary data associated with this article can be found, in the online version, at [doi:10.1016/j.jmb.2008.11.022](https://doi.org/10.1016/j.jmb.2008.11.022)

### References

- Pinto, L. H. & Lamb, R. A. (2007). Controlling influenza virus replication by inhibiting its proton channel. *Mol. Biosyst.* **3**, 18–23.
- Bright, R. A., Medina, M. J., Xu, X., Perez-Oronoz, G., Wallis, T. R., Davis, X. M. *et al.* (2005). Incidence of adamantane resistance among influenza A (H3N2) viruses isolated worldwide from 1994 to 2005: a cause for concern. *Lancet*, **366**, 1175–1181.
- Lamb, R. A., Holsinger, K. J. & Pinto, L. H. (1994). The influenza A virus M2 ion channel protein and its role in the influenza virus life cycle. In *Cellular receptors of animal viruses* (Wemmer, E., ed), pp. 303–321, Cold Spring Harbor Lab Press, Plainview, NY.
- Pinto, L. H., Holsinger, L. J. & Lamb, R. A. (1992). Influenza virus M2 protein has ion channel activity. *Cell*, **69**, 517–528.
- Holsinger, L. J., Nichani, D., Pinto, L. H. & Lamb, R. A. (1994). Influenza A virus M2 ion channel protein: a structure–function analysis. *J. Virol.* **68**, 1551–1563.
- Sakaguchi, T., Tu, Q., Pinto, L. H. & Lamb, R. A. (1997). The active oligomeric state of the minimalistic influenza virus M2 ion channel is a tetramer. *Proc. Natl Acad. Sci. USA*, **94**, 5000–5005.
- Cady, S. D. & Hong, M. (2008). Amantadine-induced conformational and dynamical changes of the influenza M2 transmembrane proton channel. *Proc. Natl Acad. Sci. USA*, **105**, 1483–1488.
- Hu, J., Fu, R., Nishimura, K., Zhang, L., Zhou, H. X., Busath, D. D. *et al.* (2006). Histidines, heart of the hydrogen ion channel from influenza A virus: toward an understanding of conductance and proton selectivity. *Proc. Natl Acad. Sci. USA*, **103**, 6865–6870.
- Tang, Y., Zaitseva, F., Lamb, R. A. & Pinto, L. H. (2002). The gate of the influenza virus M2 proton channel is formed by a single tryptophan residue. *J. Biol. Chem.* **277**, 39880–39886.
- Duff, K. C. & Ashley, R. H. (1992). The transmembrane domain of influenza A M2 protein forms amantadine-sensitive proton channels in planar lipid bilayers. *Virology*, **190**, 485–489.
- Pinto, L. H., Dieckmann, G. R., Gandhi, C. S., Papworth, C. G., Braman, J., Shaughnessy, M. A. *et al.* (1997). A functionally defined model for the M2 proton channel of influenza A virus suggests a mechanism for its ion selectivity. *Proc. Natl Acad. Sci. USA*, **94**, 11301–11306.
- Kochendoerfer, G. G., Salom, D., Lear, J. D., Wilk-Orescan, R., Kent, S. B. & DeGrado, W. F. (1999). Total chemical synthesis of the integral membrane protein influenza A virus M2: role of its C-terminal domain in tetramer assembly. *Biochemistry*, **38**, 11905–11913.
- Nguyen, P. A., Soto, C. S., Polishchuk, A., Caputo, G. A., Tatko, C. D., Ma, C. *et al.* (2008). pH-induced conformational change of the influenza M2 protein C-terminal domain. *Biochemistry*, **47**, 9934–9936.
- Schnell, J. R. & Chou, J. J. (2008). Structure and mechanism of the M2 proton channel of influenza A virus. *Nature*, **451**, 591–595.
- Stouffer, A. L., Acharya, R., Salom, D., Levine, A. S., Di Costanzo, L., Soto, C. S. *et al.* (2008). Structural basis for the function and inhibition of an influenza virus proton channel. *Nature*, **451**, 596–599.
- Miller, C. (2008). Ion channels: coughing up flu's proton channels. *Nature*, **451**, 532–533.
- Chou, J. J., Kaufman, J. D., Stahl, S. J., Wingfield, P. T. & Bax, A. (2002). Micelle-induced curvature in a water-insoluble HIV-1 Env peptide revealed by NMR dipolar coupling measurement in stretched polyacrylamide gel. *J. Am. Chem. Soc.* **124**, 2450–2451.
- Hu, J., Asbury, T., Achuthan, S., Li, C., Bertram, R., Quine, J. R. *et al.* (2007). Backbone structure of the amantadine-block trans-membrane domain M2 proton channel from influenza A virus. *Biophys. J.* **92**, 4335–4343.
- Wang, J., Kim, S., Kovacs, F. & Cross, T. A. (2001). Structure of the transmembrane region of the M2 protein H(+) channel. *Protein Sci.* **10**, 2241–2250.



20. Cady, S. D., Goodman, C., Tatko, C. D., DeGrado, W. F. & Hong, M. (2007). Determining the orientation of uniaxially rotating membrane proteins using unoriented samples: a  $^2\text{H}$ ,  $^{13}\text{C}$ , and  $^{15}\text{N}$  solid-state NMR investigation of the dynamics and orientation of a transmembrane helical bundle. *J. Am. Chem. Soc.* **129**, 5719–5729.
21. Cady, S. D. & Hong, M. (2008). Simultaneous extraction of multiple orientational constraints of membrane proteins by  $^{13}\text{C}$ -detected N–H dipolar couplings under magic angle spinning. *J. Magn. Reson.* **191**, 219–225.
22. Luo, W. & Hong, M. (2006). Determination of the oligomeric number and intermolecular distances of membrane protein assemblies by anisotropic  $(1)\text{H}$ -driven spin diffusion NMR spectroscopy. *J. Am. Chem. Soc.* **128**, 7242–7251.
23. Luo, W., Mani, R. & Hong, M. (2007). Side chain conformation and gating of the M2 transmembrane peptide proton channel of influenza A virus from solid-state NMR. *J. Phys. Chem.* **111**, 10825–10832.
24. Sansom, M. S. & Kerr, I. D. (1993). Influenza virus M2 protein: a molecular modelling study of the ion channel. *Protein Eng.* **6**, 65–74.
25. Duff, K. C., Gilchrist, P. J., Saxena, A. M. & Bradshaw, J. P. (1994). Neutron diffraction reveals the site of amantadine blockade in the influenza A M2 ion channel. *Virology*, **202**, 287–293.
26. Cornilescu, G., Delaglio, F. & Bax, A. (1999). Protein backbone angle restraints from searching a database for chemical shift and sequence homology. *J. Biomol. NMR*, **13**, 289–302.
27. de Dios, A. C. & Oldfield, E. (1994). Chemical shifts of carbonyl carbons in peptides and proteins. *J. Am. Chem. Soc.* **116**, 11485–11488.
28. Wang, J., Schnell, J. R. & Chou, J. J. (2004). Amantadine partition and localization in phospholipid membrane: a solution NMR study. *Biochem. Biophys. Res. Commun.* **324**, 212–217.
29. Li, C., Yi, M., Hu, J., Zhou, H. X. & Cross, T. A. (2008). Solid-state NMR and MD simulations of the antiviral drug amantadine solubilized in DMPC bilayers. *Biophys. J.* **94**, 1295–1302.
30. Subczynski, W. K., Wojas, J., Pezeshk, V. & Pezeshk, A. (1998). Partitioning and localization of spin-labeled amantadine in lipid bilayers: an EPR study. *J. Pharm. Sci.* **87**, 1249–1254.
31. Li, C., Qin, H., Gao, F. P. & Cross, T. A. (2007). Solid-state NMR characterization of conformational plasticity within the transmembrane domain of the influenza A M2 proton channel. *Biochim. Biophys. Acta*, **1768**, 3162–3170.
32. O'Neil, K. T. & DeGrado, W. F. (1990). A thermodynamic scale for the helix-forming tendencies of the commonly occurring amino acids. *Science*, **250**, 646–651.
33. Javadpour, M. M., Eilers, M., Groesbeek, M. & Smith, S. O. (1999). Helix packing in polytopic membrane proteins: role of glycine in transmembrane helix association. *Biophys. J.* **77**, 1609–1618.
34. Howard, K. P., Lear, J. D. & DeGrado, W. F. (2002). Sequence determinants of the energetics of folding of a transmembrane four-helix-bundle protein. *Proc. Natl Acad. Sci. USA*, **99**, 8568–8572.
35. Buffy, J. J., Waring, A. J. & Hong, M. (2005). Determination of peptide oligomerization in lipid membranes with magic-angle spinning spin diffusion NMR. *J. Am. Chem. Soc.* **127**, 4477–4483.
36. Harris, N. L., Presnell, S. R. & Cohen, F. E. (1994). Four helix bundle diversity in globular proteins. *J. Mol. Biol.* **236**, 1356–1368.
37. Duong-Ly, K. C., Nanda, V., DeGrado, W. F. & Howard, K. P. (2005). The conformation of the pore region of the M2 proton channel depends on lipid bilayer environment. *Protein Sci.* **14**, 856–861.
38. Neal, S., Nip, A. M., Zhang, H. & Wishart, D. S. (2003). Rapid and accurate calculation of protein  $^1\text{H}$ ,  $^{13}\text{C}$  and  $^{15}\text{N}$  chemical shifts. *J. Biomol. NMR*, **26**, 215–240.
39. Le, H. & Oldfield, E. (1994). Correlation between  $^{15}\text{N}$  NMR chemical shifts in proteins and secondary structure. *J. Biomol. NMR*, **4**, 341–348.
40. deDios, A. C., Pearson, J. G. & Oldfield, E. (1993). Secondary and tertiary structural effects on protein NMR chemical shifts: an ab initio approach. *Science*, **260**, 1491–1496.
41. Zhang, H., Neal, S. & Wishart, D. S. (2003). RefDB: a database of uniformly referenced protein chemical shifts. *J. Biomol. NMR*, **25**, 173–195.
42. Jing, X., Ma, C., Ohigashi, Y., Oliveira, F. A., Jardetzky, T. S., Pinto, L. H. & Lamb, R. A. (2008). Functional studies indicate amantadine binds to the pore of the influenza A virus M2 proton-selective ion channel. *Proc. Natl Acad. Sci. USA*, **105**, 10967–10972.
43. Lovell, S. C., Word, J. M., Richardson, J. S. & Richardson, D. C. (2000). The penultimate rotamer library. *Proteins: Struct., Funct., Genet.* **40**, 389–408.
44. Carpino, L. A. & Han, G. Y. (1972). 9-Fluorenylmethoxycarbonyl amino-protecting group. *J. Org. Chem.* **37**, 3404–3409.
45. Ito, T., Gorman, O. T., Kawaoka, Y., Bean, W. J. & Webster, R. G. (1991). Evolutionary analysis of the influenza A virus M gene with comparison of the M1 and M2 proteins. *J. Virol.* **65**, 5491–5498.
46. Traikia, M., Warschawski, D. E., Recouvreur, M., Cartaud, J. & Devaux, P. F. (2000). Formation of unilamellar vesicles by repetitive freeze–thaw cycles: characterization by electron microscopy and  $^{31}\text{P}$ -nuclear magnetic resonance. *Eur. Biophys. J.* **29**, 184–195.
47. Bennett, A. E., Rienstra, C. M., Auger, M., Lakshmi, K. V. & Griffin, R. G. (1995). Heteronuclear decoupling in rotating solids. *J. Chem. Phys.* **103**, 6951–6958.
48. Fung, B. M., Khitrin, A. K. & Ermolaev, K. (2000). An improved broadband decoupling sequence for liquid crystals and solids. *J. Magn. Reson.* **142**, 97–101.
49. Hohwy, M., Rienstra, C. M., Jaroniec, C. P. & Griffin, R. G. (1999). Fivefold symmetric homonuclear dipolar recoupling in rotating solids: application to double-quantum spectroscopy. *J. Chem. Phys.* **110**, 7983–7992.
50. Takegoshi, K., Nakamura, S. & Terao, T. (2001). C-13–H-1 dipolar-assisted rotational resonance in magic-angle spinning NMR. *Chem. Phys. Lett.* **344**, 631–637.
51. Bax, A., Freeman, R. & Kempell, S. P. (1980). Natural-abundance  $^{13}\text{C}$ – $^{13}\text{C}$  coupling observed via double-quantum coherence. *J. Am. Chem. Soc.* **102**, 4849–4851.
52. Hong, M. (1999). Solid-state dipolar INADEQUATE NMR spectroscopy with a large double-quantum spectral width. *J. Magn. Reson.* **136**, 86–91.
53. Gullion, T. & Schaefer, J. (1989). Rotational echo double resonance NMR. *J. Magn. Reson.* **81**, 196–200.
54. Hong, M. & Griffin, R. G. (1998). Resonance assignment for solid peptides by dipolar-mediated  $^{13}\text{C}/^{15}\text{N}$  correlation solid-state NMR. *J. Am. Chem. Soc.* **120**, 7113–7114.
55. Mao, J. D. & Schmidt-Rohr, K. (2005). Methylene spectral editing in solid-state C-13 NMR by three-spin coherence selection. *J. Magn. Reson.* **176**, 1–6.
56. Rhim, W.-K., Elleman, D. D. & Vaughan, R. W. (1973). Analysis of multiple-pulse NMR in solids. *J. Chem. Phys.* **59**, 3740–3749.